Cement and Concrete Composites 74 (2016) 71–87

Contents lists available at ScienceDirect

Cement and Concrete Composites

journal homepage: www.elsevier.com/locate/cemconcomp

Predicting the flexural behavior of ultra-high-performance fiber-reinforced concrete

Doo-Yeol Yoo [a], Nemkumar Banthia [b], Young-Soo Yoon [c, *]

[a] Department of Architectural Engineering, Hanyang University, 222 Wangsimni-ro, Seongdong-gu, Seoul 04763, Republic of Korea
[b] Department of Civil Engineering, The University of British Columbia, 6250 Applied Science Lane, Vancouver, BC V6T 1Z4, Canada
[c] School of Civil, Environmental and Architectural Engineering, Korea University, 145 Anam-ro, Seongbuk-gu, Seoul 02841, Republic of Korea

ARTICLE INFO

Article history:
Received 6 September 2015
Received in revised form
23 June 2016
Accepted 8 September 2016
Available online 9 September 2016

Keywords:
Ultra-high-performance fiber-reinforced concrete
Fiber length
Flexure
Micromechanical modeling
Tension-softening curve
Sectional analysis

ABSTRACT

To predict the flexural behavior of ultra-high-performance fiber-reinforced concrete (UHPFRC) beams including straight steel fibers with various lengths, micromechanics-based sectional analysis was performed. A linear compressive modeling was adopted on the basis of experiments. The tensile behavior was modeled by considering both pre- and post-cracking tensile behaviors. Pre-cracking behavior was modeled by the rule of mixture. Post-cracking behavior was modeled by a bilinear matrix softening curve and fiber bridging curves, considering three different probability density functions (PDFs) for fiber orientation, i.e., the actual PDF from image analysis and PDFs assuming either random two-dimensional (2-D) or three-dimensional (3-D) fiber orientation. Analytical predictions using the fiber bridging curves with the actual PDF or the PDF assuming 2-D random fiber orientation showed fairly good agreement with the experimental results, whereas analysis using the PDF assuming 3-D random fiber orientation greatly underestimated the experimental results.

1. Introduction

Over the past decades, concrete has been recognized as one of the most widely used construction materials, owing to its remarkable compressive strength, durability, and cost-effectiveness. However, its relatively low tensile strength, poor energy absorption capacity, and brittle failure have hindered its application in structures subjected to tension-dominated loads and extreme loads, such as earthquakes, impacts, and blasts. Among the various methods to overcome these drawbacks, fiber reinforcements have been adopted by many researchers. Fiber reinforcement is the simplest and most effective way to enhance fracture toughness through the strengthened post-cracking stress transfer capability in concrete [1–4]. Post-cracking tensile behavior is illustrated for conventional concrete and fiber-reinforced concrete (FRC) (in Fig. 1) [5]. Fibers crossing the crack planes transfer the load to the concrete, and thus, significantly improved post-cracking tensile performances including higher load carrying capacity and ductility are obtained for FRC in comparison with conventional concrete or matrix.

Ultra-high-performance fiber-reinforced concrete (UHPFRC) was first developed in mid-1990s. It has attracted much attention from engineers due to its excellent strength (compressive strength is higher than 150 MPa and tensile strength is equal to or higher than 8 MPa), ductility, and fatigue resistance, as well as a unique strain-hardening response involving multiple micro-cracks [6,7]. In recent years, several studies [8–12] have been carried out to more improve its tensile or flexural performance at identical fiber volume fractions by using various types of steel fibers. Wille et al. [9] experimentally verified that the use of twisted steel fiber improved the post-cracking tensile strength and strain capacity, compared to that of short straight steel fiber, which is used for commercial UHPFRC available in North America [13]. In addition, Yoo et al. [12] reported that the use of longer straight steel fibers with a higher aspect ratio provided much improved flexural performance including strength, deflection capacity, and energy absorption capacity than that of short ones, because of their higher effective bonding area between the fiber and matrix and higher possibility of locating the fibers at the crack surfaces. Thus, the addition of both deformed (twisted) and long straight steel fibers is effective in improving the tensile or flexure performance, but the

* Corresponding author.
E-mail addresses: dyyoo@hanyang.ac.kr (D.-Y. Yoo), banthia@civil.ubc.ca (N. Banthia), ysyoon@korea.ac.kr (Y.-S. Yoon).

http://dx.doi.org/10.1016/j.cemconcomp.2016.09.005
0958-9465/

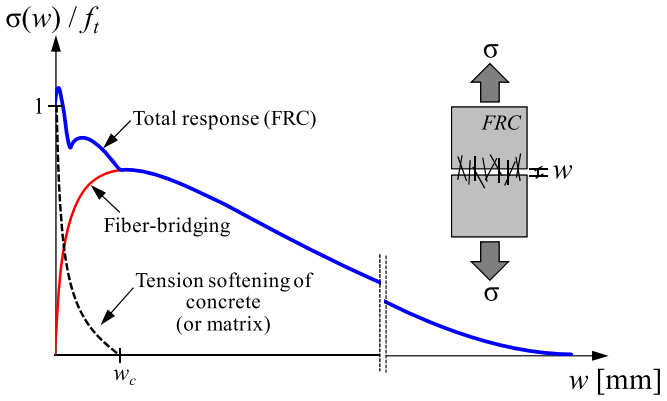

Fig. 1. Conceptual view of post-cracking tensile behavior of FRC [5].

use of long straight steel fiber is preferred for the case of UHPFRC because it is simpler to be fabricated and exhibits better resistance at high rate loadings [14].

In order to precisely analyze the response of UHPFRC elements subjected to tension or flexure, a realistic tensile model including fiber bridging and matrix softening curves are required. Bažant and Planas [15] reported that *true* tensile test is difficult to carry out, because of either rotation of the supports or internal elastic rotation in the specimen itself, and sophisticated machine needs to minimize the rotation. For the limitation, some researchers [11,16] have proposed the tensile model of UHPFRC based on the numerical approach. Habel et al. [17] successfully predicted the structural behavior of composite UHPFRC–concrete beams on the basis of an analytical cross-sectional model developed. Wille et al. [18] predicted the flexural behavior of UHPFRC based on the backward analysis considering the fiber orientation and dispersion along the beam height and reported that the fiber orientation and distribution over the height of beam give marginal effect on the numerical results. Yoo et al. [12] also simulated the flexural behavior of UHPFRC beams with various steel fibers and placement methods, based on the fracture mechanics-based inverse analysis, and they suggested a generalized tension-softening model. However, it required indirect tensile tests and very complicated program code to carry out the inverse analysis, thus a substitutive micromechanical analysis was adopted by Kang and Kim [16] to predict the uniaxial tensile response of UHPFRC reinforced with 2% by volume of short straight steel fibers (l_f/d_f = 13/0.2 mm/mm, where l_f is the fiber length and d_f is the fiber diameter). Based on their analysis [16], the post-cracking tensile behavior was reasonably simulated using only restrictive fundamental information, such as a single fiber pullout model, matrix softening curve, and probability density function (PDF) of fiber orientation. Likewise, various numerical methods for predicting structural and mechanical responses of UHPFRC have been developed by several researchers.

Various simple bi or trilinear tension-softening models were proposed for UHPFRC [12,19–22]. Japan Society of Civil Engineers (JSCE) [19], Habel and Gauvreau [20], and Yoo et al. [21] proposed bilinear tension-softening models for UHPFRC incorporating short straight steel fibers with various coefficients, while Kang et al. [22] and Yoo et al. [12] suggested trilinear tension-softening models for various types of UHPFRC with different volume fractions and lengths of straight steel fibers. However, not only did they suggest the tension-softening models based on their own test data, but also there is no published study, which comprehensively compares the previous models and examines their applicability in prediction of flexural behavior of UHPFRC with various fibers.

Accordingly, in this study, to predict the flexural response of UHPFRC containing steel fibers of various lengths and different fiber orientations, a micromechanics-based analytical technique was adopted. For this, a tension-softening curve consisting of matrix softening and fiber bridging curves considering randomly oriented multiple fibers was suggested, and subsequently, a sectional analysis was performed incorporating linear compressive and pre-cracking tensile models as well as the suggested tension-softening curve. The previously suggested tension-softening models were also adopted, and their predictive values obtained by sectional analyses were verified through comparison with the test data.

Table 2
Chemical compositions and physical properties of cementitious materials.

Composition % (mass)	Cement	Silica fume
CaO	61.33	0.38
Al_2O_3	6.40	0.25
SiO_2	21.01	96.00
Fe_2O_3	3.12	0.12
MgO	3.02	0.10
SO_3	2.30	–
Specific surface (cm^2/g)	3413	200,000
Density (g/cm^3)	3.15	2.10

2. Experimental section

2.1. Mixture proportions and test set-up

The mix proportions used in this study are summarized in Table 1. For cementitious materials, Type 1 Portland cement and silica fume were used. The chemical compositions and physical properties of these materials are given in Table 2. Silica flour with a diameter of 2 μm including 98% SiO_2 and silica sand with a grain size of less than 0.5 mm were included. Coarse aggregate was excluded from the mixture to improve its homogeneity. A water-to-binder ratio (W/B) of 0.2 was used, and 1.6% of liquid type polycarboxylate superplasticizer with a solid content of 30% was added to obtain proper fluidity and viscosity. To estimate the effect of fiber length on the flexural behavior, three types of steel fibers with different lengths, l_f, of 13, 16.3, and 19.5 mm and a constant diameter, d_f, of 0.2 mm, leading to three different fiber aspect ratios, l_f/d_f, of 65, 81.5, and 97.5, were included by 2% by volume. The commercial UHPFRC available in North America contains 2% by volume of steel fibers with l_f/d_f = 13/0.2 mm/mm = 65 [13]. The properties of steel fibers are given in Table 3. Test specimens were fabricated by pouring concrete from the corner and letting it to flow naturally.

Table 1
Mix proportions.

W/B (%)	Unit weight (kg/m^3)						Flow (mm)
	Water	Cement	Silica fume	Silica flour	Silica sand	SP (%)	
20	160.3	788.5	197.1	236.6	867.4	1.6	230–240

[Note] SP = superplasticizer.

Table 3
Properties of steel fibers.

Name	Diameter, d_f (mm)	Length, l_f (mm)	Aspect ratio (l_f/d_f)	Density (g/cm^3)	Tensile strength (MPa)	Elastic modulus (GPa)
S13	0.2	13.0	65.0	7.8	2500	200
S16.3	0.2	16.3	81.5			
S19.5	0.2	19.5	97.5			

Table 4
Summary of mechanical test results.

Name	f_c' (MPa)	E_c (MPa)	P_{MOR} (kN)	δ_{MOR} (mm)	$CMOD_{MOR}$ (mm)
S13	201.8 (2.14)	50876 (545.0)	27.9 (1.27)	0.49 (0.041)	0.61 (0.059)
S16.3	204.5 (1.63)	46260 (166.0)	32.9 (3.21)	0.75 (0.107)	1.00 (0.243)
S19.5	197.3 (0.89)	46126 (878.1)	37.9 (2.05)	1.31 (0.365)	1.88 (0.547)

[Note] f_c' = compressive strength, E_c = elastic modulus, P_{MOR} = peak flexural load.
δ_{MOR} = deflection at the peak load, $CMOD_{MOR}$ = CMOD at the peak load, and (x.xxx) = standard deviation.

A total of nine cylindrical specimens (three cylinders for each variable) with a diameter of 100 mm and a length of 200 mm were fabricated and tested as per ASTM C 39 [23]. A uniaxial compressive load was applied from a universal testing machine (UTM) with a maximum capacity of 3000 kN at a loading rate of 0.1 mm/min. In addition, a compressometer equipped with three linear variable differential transformers (LVDTs) was used to measure the average compressive strain and elastic modulus with a gage length of 100 mm. The average parameters characterizing the compressive performance such as compressive strength and elastic modulus are summarized in Table 4.

A three-point flexure test was performed as per JCI-S-002-2003 standard [24]. In the JCI standard, the side length of the cross-section of beam is recommended to be larger than 100 mm. Therefore, the beam specimens with cross-sectional dimensions of 100 × 100 mm and a length of 400 mm were adopted. In addition, as per the JCI standard, a 30-mm notch was adopted at the mid-length of the specimen. Nine beams (three beams for each variable) were fabricated and tested. A load was applied using a UTM with a maximum load capacity of 250 kN through displacement control. A clear span of 300 mm was used, and two LVDTs were installed on both sides of the specimen for the center deflection measurement. In addition, to measure the crack mouth opening displacement (CMOD), a clip gauge with a capacity of 10 mm was located at the notch, as shown in Fig. 2. The details of the test set-up and procedure for both compressive and flexural tests can be found elsewhere [12].

The letter S denotes the incorporation of steel fiber and the subsequent numeral indicates the fiber length. For example, S19.5 refers to the specimens including 2 vol% of steel fibers, having a length of 19.5 mm.

2.2. Flexural test results

Fig. 3 shows the average flexural load-CMOD behaviors of UHPFRC beams as a function of the fiber length. All reported test results shown were obtained by averaging the results from three beams based on a linear interpolation, which is similar to the method used in a previous study [25]. In addition, the average parameters characterizing the flexural performance are given in Table 4. The initial slope and descending slope in the load-CMOD curves were not significantly affected by the fiber length, whereas the peak load, deflection capacity, and CMOD at the peak were noticeably improved by an increase in the fiber length, on account of the increase of bonding area between the fiber and matrix with an insignificant change in the number of fibers at the cracked section. For example, the highest peak load was found to be 37.9 kN for the specimen S19.5, which was approximately 15% and 36% higher than those of the specimens S16.3 and S13, respectively. All test series generated a higher load carrying capacity after matrix cracking and exhibited only one major crack at the center of the span due to the notch, as shown in Fig. 4.

2.3. Discussion on tensile performance

Fig. 5 exhibits the average direct tensile stress-strain curves of UHPFRC with fiber lengths of 13 and 19.5 mm, reported by Yoo et al. [26]. Specimen S19.5 provided better tensile performance, such as higher tensile strength, strain capacity and more micro-cracks, than those of the specimen S13, similar to the flexural test results. Thus, it can be noted that the use of long steel fibers is effective in improving tensile performance of UHPFRC. All test specimens showed "strain-hardening response", $f_{LOP,t} < f_{MOR,t}$, where $f_{LOP,t}$ is the first cracking tensile strength and $f_{MOR,t}$ is the post-cracking

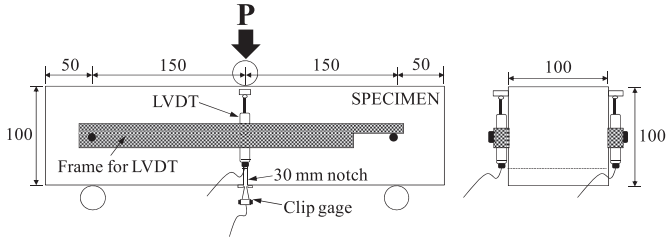

Fig. 2. Test setup for three-point flexure test of notched beam (unit: mm).

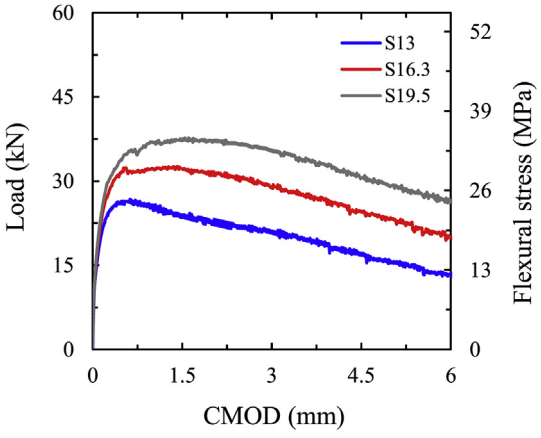

Fig. 3. Average load-CMOD curves.

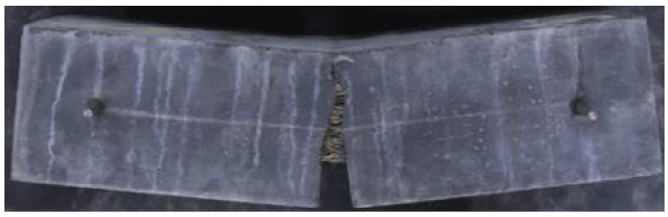

Fig. 4. Typical failure mode of UHPFRC beam (S19.5).

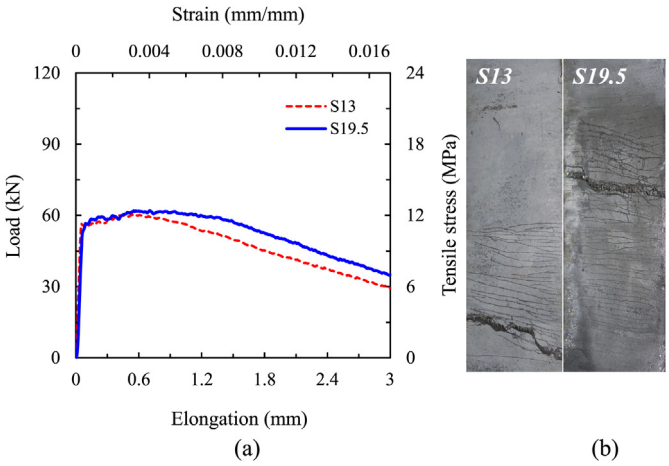

Fig. 5. Direct tensile behaviors [26]; (a) stress versus strain curves, (b) cracking behaviors.

tensile strength. Based on the discussion following the 2003 fourth international workshop on High Performance Fiber Reinforced Cement Composites (HPFRCC-4), the tensile strain-hardening composite is considered to have mechanically more performance than the strain-softening one, and thus, it is useful in structural applications where tensile or flexure prevails [27]. However, since the post-cracking tensile response, as given in Fig. 5, was more dominated by softening behavior and the difference between $f_{LOP,t}$ and $f_{MOR,t}$ was insignificant, the combined matrix softening and fiber bridging curve was named as a "tension-softening curve", adopted by several international recommendations for UHPFRC [19,28], rather than a "tension-hardening curve."

2.4. Image analysis results

Fig. 6 shows the binary images obtained in the maximum moment region at the center of the UHPFRC beams with three different fiber lengths. The procedure for obtaining binary images and the equations for calculating the fiber orientation and dispersion parameters can be found elsewhere [12]. Due to the wall effect, the fibers near the wall tended to be more aligned with the direction of flow than those farther from the wall. Several parameters characterizing the fiber distribution, such as the fiber dispersion coefficient, the number of fiber per unit area, the fiber orientation coefficient, and the fiber number coefficient, are summarized in Table 5. The fiber dispersion coefficient and the number of fibers per unit area were insignificantly affected by the fiber length, whereas the fiber orientation coefficient decreased with an increase in the fiber length. This is caused by the fact that since the reduction of aspect ratio increased the effective viscosity and decreased the drag reduction efficiency, the magnitude of fiber-orienting torque was improved [29,30]. This is consistent with the findings from Yoo et al. [25] that in the case of radial flow, better fiber orientation was obtained by using steel fibers with a shorter length.

Table 5
Fiber orientation and dispersion coefficients at the center of beam.

Name	α_f	F_n (number/mm^2)	η_θ	α_{nf}
S13	0.394	0.340	0.612	0.696
S16.3	0.388	0.331	0.578	0.689
S19.5	0.395	0.358	0.553	0.770

[Note] α_f = fiber dispersion coefficient, F_n = number of fiber per unit area, η_θ = fiber orientation coefficient, and α_{nf} = fiber number coefficient.

As shown in Fig. 7, the PDF obtained from the image analysis differs from those obtained by the assumptions of two-dimensional (2-D) and three-dimensional (3-D) random fiber orientations. The PDF of 3-D random fiber orientation was obtained by assuming that the fiber ends lying on the hemispherical surface, reported by Li et al. [31]. The actual PDF is skewed to the right with increasing the fiber length. Thus, shorter fibers tend to be more aligned with the direction of flow than longer fibers.

3. Micromechanical modeling to predict the flexural response of UHPFRC beams

3.1. Pre-cracking tensile modeling

Before cracking occurs in FRCs, applied external tensile load is transferred from the matrix, which has a low elastic modulus, to the fiber, which has a high elastic modulus, via shear transfer mechanism. Thus, part of the load is carried by the fibers and the rest by the matrix. This interaction between the fiber and the matrix is

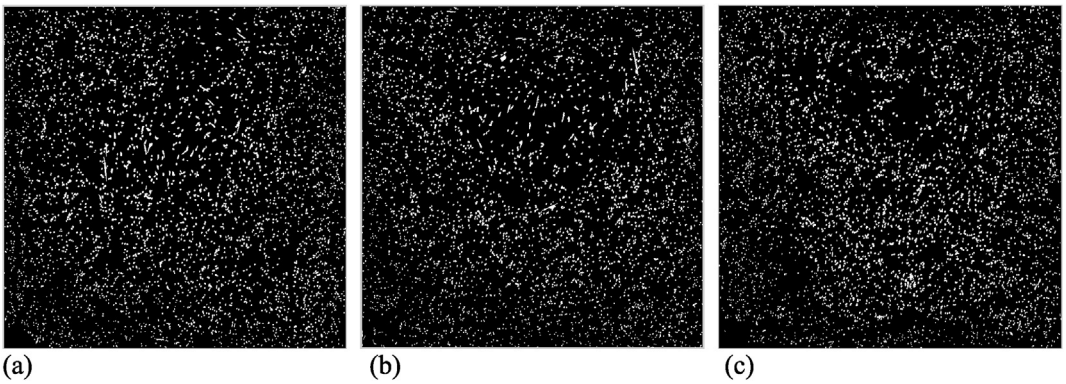

Fig. 6. Binary images at the crack surfaces; (a) S13, (b) S16.3, (c) S19.5.

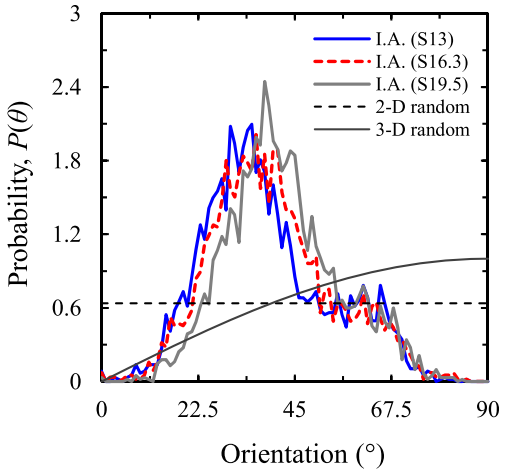

Fig. 7. PDF for fiber orientation according to fiber length (Note: I.A. indicates the Image Analysis).

elastic in nature during the early stages of loadings. The shear stress is non-uniformly distributed along the embedment length. A schematic deformation around the fiber and shear stress distribution is shown in Fig. 8 [1]. Cox [32] first developed analytical models for the tensile stress $\sigma_f(x)$ in the fiber and the elastic shear stress at the interface $\tau(x)$ at a distance of x from the fiber end, as follows:

$$\sigma_f(x) = E_f\varepsilon_m\left\{\frac{1-\cosh\beta_1\left(\frac{l_f}{2}-x\right)}{\cosh\frac{\beta_1 l_f}{2}}\right\} \tag{1}$$

$$\tau(x) = E_f\varepsilon_m\left\{\frac{G_m}{2E_f\ln\left(R_m/r_f\right)}\right\}^{1/2}\frac{\sinh\beta_1\left(\frac{l_f}{2}-x\right)}{\cosh\frac{\beta_1 l_f}{2}} \tag{2}$$

Here,

$$\beta_1 = \left\{\frac{2G_m}{E_f r_f^2\ln\left(R_m/r_f\right)}\right\}^{1/2} \tag{3}$$

where E_f is the elastic modulus of the fiber, ε_m is the local strain of the matrix,G_m is the shear modulus of the matrix at the interface ($G_m = E_m/2(1+\nu_m)$), ν_m is the Poisson's ratio of the matrix, R_m is the radius of the matrix around the fiber, and r_f is the radius of the fiber. Herein, R_m/r_f depends on the fiber packing and the volume contents of the fibers. For long fibers with a circular cross-section, the following equations can be adopted [33]:

$$\text{For square packing} \;:\; \ln\left(R_m/r_f\right) = \frac{1}{2}\ln\left(\pi/V_f\right) \tag{4}$$

$$\text{For hexagonal packing} \;:\; \ln\left(R_m/r_f\right) = \frac{1}{2}\ln\left[2\pi\Big/\left(3V_f\right)^{1/2}\right] \tag{5}$$

where V_f is the volume fraction of fiber. Hexagonal packing was used in this study, similar to a previous research by Kang and Kim [16].

The tensile stress in FRC can be calculated by the 'rule of mixture', as applying Eqs. (6)–(8). The existence of a uniform strain is assumed throughout the FRC. Failure occurs when either the fiber or the matrix reaches the failure strain.

$$\sigma_c(\varepsilon_c) = \sigma_m(\varepsilon_c)V_m + \eta_l\eta_\theta\sigma_f(\varepsilon_c)V_f \tag{6}$$

where

$$\eta_l = 1 - \frac{\tanh\left(\beta_1 l_f/2\right)}{\left(\beta_1 l_f/2\right)} \tag{7}$$

$$\eta_\theta = \int_{\theta_{\min}}^{\theta_{\max}} p(\theta)\cos^2\theta\, d\theta \tag{8}$$

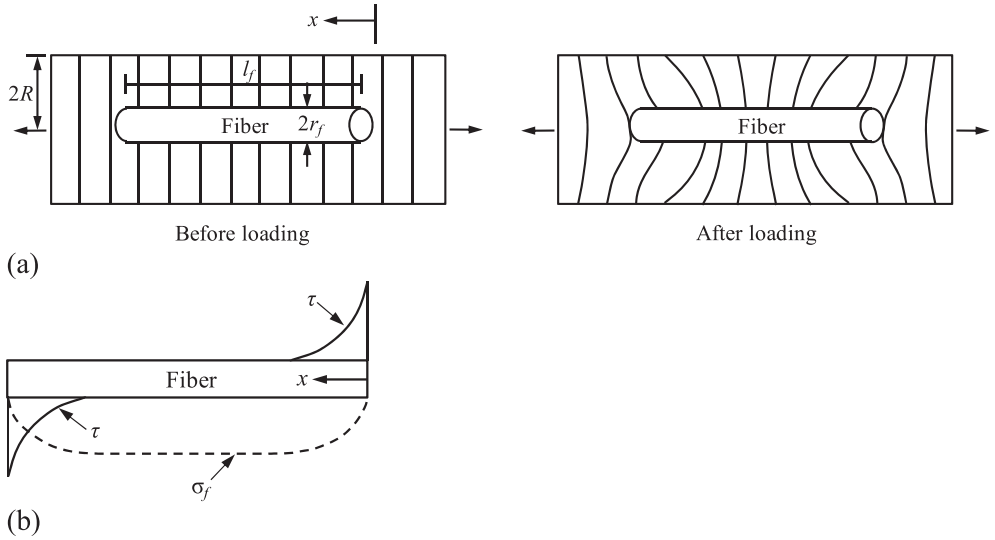

Fig. 8. Schematic view of the deformation and stress fields around the fiber; (a) geometry of the fiber and the deformation in the matrix around the fiber before and after loading, (b) elastic shear stress distribution at the interface and tensile stress distribution in the fiber [1].

where σ_c is the stress in FRC, σ_m is the stress in the matrix, ε_c is the strain in FRC, V_m is the volume fraction of the matrix, η_l is the length efficiency factor in the pre-cracking case for the frictional stress transfer mechanism, η_θ is the fiber orientation coefficient, σ_f is the stress in the fiber, θ is the inclination angle of the fiber with respect to the loading direction, and $p(\theta)$ is the PDF for fiber orientation. Herein, $\eta_\theta = 2/\pi$ for 2-D random fiber orientation and $\eta_\theta = 1/2$ for 3-D random fiber orientation, respectively.

Eq. (8) is derived by assuming that no enhancement in the tensile strength is achieved when all fibers are aligned perpendicular to the loading direction, whereas the tensile strength is maximized when fibers are all aligned parallel to the loading direction. Thus, $\eta_\theta = 1$ denotes that all fibers are aligned parallel to the loading direction, and conversely, $\eta_\theta = 0$ indicates that all fibers are aligned perpendicular to the loading direction.

3.2. Post-cracking tensile modeling

3.2.1. Snubbing and matrix spalling effects

Li et al. [34] indicated that the bond strength of synthetic fibers increases when the fibers are inclined in the tensile load direction, and this is caused by a result of the local interaction forces (matrix reaction force R and friction force μR) between the fiber and the matrix at the exit point, as shown in Fig. 9. This is named as the '*snubbing effect*'. Due to the snubbing effect, the bond strength of straight steel fibers in ultra-high strength cementitious matrix increased with the increase of inclination angle up to 45°. The largest bond strength was obtained between an angle of 30° and 45° [35]. On the other hand, in the case of deformed steel fibers embedded in normal-, medium-, and high-strength concretes, the fibers that were aligned in the direction of loading exhibited higher pullout resistance than the fibers inclined with respect to the loading direction [36]. In addition, Schauffert et al. [37] reported that the snubbing effect is not as strong for the steel fibers as compared with the polyvinyl alcohol (PVA) fibers. Since the fiber pullout behavior is strongly influenced by the inclination angle and different according to fiber type and matrix strength, a further study to comprehensively investigate the snubbing effect on fiber pullout behavior is required to be done. A local failure of the matrix also occurs at the matrix wedge due to stress concentration from the pullout load of the inclined fiber and leads to a drop of pullout load as well as an increase of crack opening displacement (COD). This is the '*matrix spalling effect*'. In the case of inclined steel fiber, the gradual spalling of the matrix occurs together with the snubbing effect. Thus, the combined effects of the snubbing and matrix spalling need to be considered when modeling the pullout behavior of an inclined single fiber.

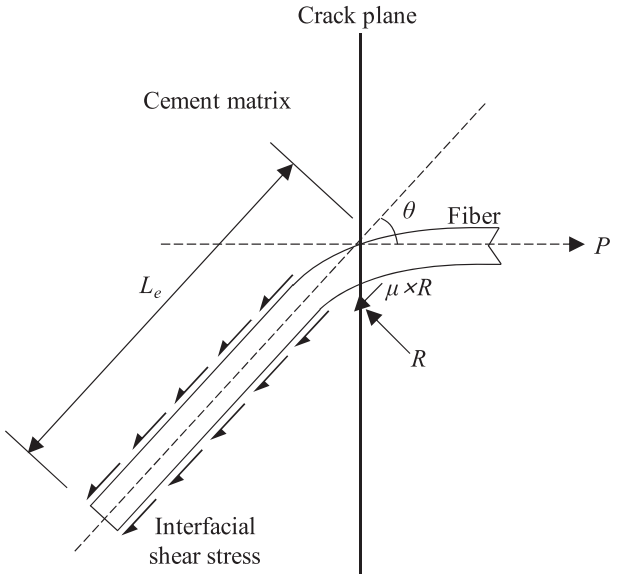

Fig. 9. Schematic description of crack bridging of obliquely aligned fiber (Kanda and Li [38]).

By considering these effects on bond behavior and replacing pullout load with stress, the apparent bond strength and frictional shear strength ($\tau_{\max(app)}$ and $\tau_{f(app)}$) can be expressed as a function of inclination angle, as follows:

$$\tau_{\max(app)}(\theta) = \tau_{f(app)}(\theta) = e^{f\theta}(\cos\theta)^k \tau(\theta = 0) \tag{9}$$

where f and k are coefficients describing the increase of bond and frictional shear strengths, respectively, as a function of inclination angle. The comparison of the measured and predicted apparent bond strengths is shown in Fig. 10(a). The coefficients f and k were calculated to be 1.6 and 1.8, respectively. Eq. (9) showed good agreement with the previous experimental results [35].

In order to take into account the increase in the slip capacity (slip at the peak strength) with increasing inclination angle of the fiber, the coefficient β is also adopted, as follows (Fig. 10(b)):

$$\delta(\theta) = \beta\delta(\theta = 0) \tag{10}$$

Here,

$$\beta = 1 + \gamma\left(\frac{2\theta}{\pi}\right)^n \tag{11}$$

where δ is the slip displacement and γ and n are the coefficients for considering the increase of slip capacity with the inclination angle. $\gamma = 100$ and $n = 2$ were adopted as calculated by Lee et al. [35].

In general, the apparent tensile strength of polyvinyl alcohol (PVA) fiber decreases with the inclination angle, because the interaction between the fiber and the matrix at the exit point led to an additional stress by bending. However, in contrast to PVA fibers [38], the steel fibers did not break before being completely pulled out in this study. This is because the steel fibers are much stiffer in bending than PVA fibers. The fiber pullout test results obtained by Yoo et al. [6] reported the maximum stresses of 981.1 MPa and 1507.1 MPa in straight 13 and 19 mm-long steel fibers embedded in ultra-high-strength matrix. These values are just 39% and 60% of the fiber tensile strength of 2500 MPa. Because of these observations, the degraded fiber tensile strength (apparent fiber strength) was not considered.

3.2.2. Pullout modeling of a single fiber embedded in an ultra-high-strength cementitious matrix

The pullout behavior of straight steel fiber embedded in a cementitious matrix consists of (a) a perfect bonding region, (b) a partial debonding region, and (c) a full debonding region. Categories (a) and (b) are included in the ascending part of the pullout load-slip curve, while category (c) is included in the descending part, as shown in Fig. 11. The mathematical equations for predicting the pullout behavior of straight steel fibers were first suggested by Naaman et al. [39]. Based on these equations, Lee et al. [35] suggested a modified analytical model to simulate the pullout response of straight steel fibers embedded in an ultra-high-strength cementitious matrix having almost identical properties to that used in this study. In their study, modeling the ascending part was mostly based on Naaman's equation, but the frictional shear stress was assumed to be identical to the bond strength. The descending part can be modeled by the assumption that the frictional shear

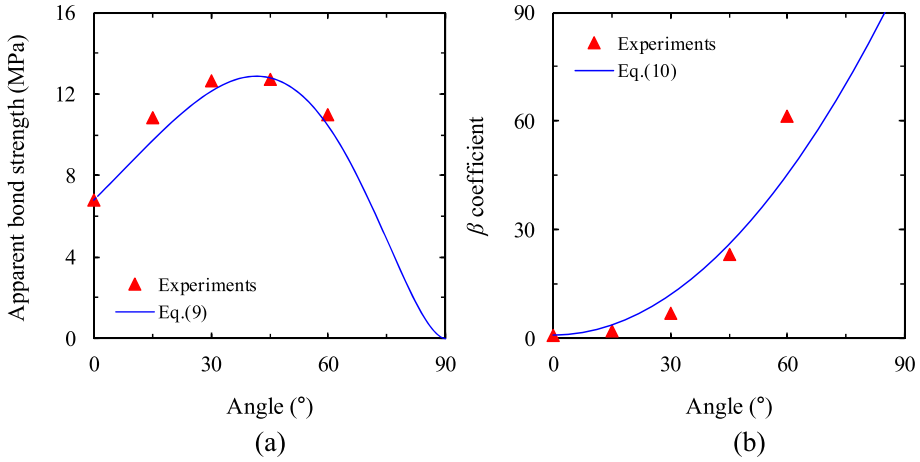

Fig. 10. Comparison of experiments and predicted values for; (a) apparent bond strength, (b) β coefficient [35].

stress decays with increasing the slip. Naaman et al. [39] adopted an exponential function to model the decayed frictional shear stress of the fibers embedded in normal- and high-strength cementitious matrices due to a fiber-matrix misfit (an asymptotic decaying model). However, Lee et al. [35] experimentally verified that the pullout response of straight steel fibers embedded in an ultra-high-strength cementitious matrix is totally different from the asymptotic decaying model using an exponential function. A new empirical model for slip softening behavior of straight steel fibers in an ultra-high-strength cementitious matrix was suggested.

The complete pullout load-slip models for single straight steel fibers in an ultra-high-strength cementitious matrix with various inclination angles are expressed by the following Eqs. (12)–(20). The detailed derivation of these equations can be found elsewhere [8].

(a) A perfect bonding region in ascending branch, before the critical pullout load when the shear stress acting on the fiber and matrix at $x = l$ reaches its bond strength ($P \le P_{crit}$).

$$\left(\frac{P}{\delta}\right)(\theta) = \frac{1/2}{1+\gamma\left(\frac{2\theta}{\pi}\right)^n}\,\frac{\lambda A_m E_m}{Q-2}\,\frac{1+e^{-\lambda l}}{1-e^{-\lambda l}} \tag{12}$$

where

$$\lambda = \sqrt{KQ} \tag{13}$$

$$K = \frac{\pi d_f \kappa}{A_m E_m} \tag{14}$$

$$Q = 1 + \frac{A_m E_m}{A_f E_f} \tag{15}$$

where P is the pullout load, A_m and E_m are the area and elastic modulus of the matrix, respectively, l is the embedment length, κ is the initial slope of the bond stress–slip relation, and A_f is the area of the fiber.

(b) A partial debonding region in the ascending branch, after the critical pullout load when the shear stress acting on the fiber and matrix at $x = l$ reaches its bond strength ($P > P_{crit}$) and before the complete debonding of the interface.

$$P(\theta) = \pi d_f \tau_{f(\mathrm{app})}(\theta) u + \frac{\pi d_f \tau_{\max(\mathrm{app})}(\theta)}{\lambda}\,\frac{1-e^{-2\lambda(l-u)}}{\frac{2}{Q}e^{-\lambda(l-u)} + \left(1-\frac{1}{Q}\right)\left[1+e^{-2\lambda(l-u)}\right]} \tag{16}$$

$$\delta(\theta) = \left[1+\gamma\left(\frac{2\theta}{\pi}\right)^n\right]\frac{2}{A_m E_m}\left\{P(\theta)(Q-1)u - \frac{\pi d_f \tau_{f(\mathrm{app})}(\theta) u^2}{2}(Q-2) + \left(P(\theta) - \pi d_f \tau_{f(\mathrm{app})}(\theta) u\right) \times \left[\frac{1-e^{-\lambda(l-u)}}{1+e^{-\lambda(l-u)}}\right]\frac{Q-2}{\lambda} - \pi d_f \tau_{f(\mathrm{app})}(\theta) u l\right\} \tag{17}$$

where u is the length of the debonding zone.

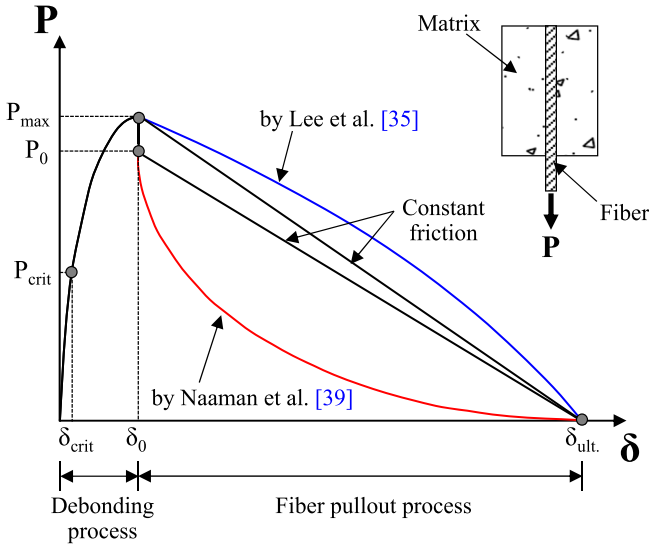

Fig. 11. Schematic description of pullout behaviors of straight steel fiber in cementitious matrix.

(c) A full debonding region in the descending branch, after complete debonding of the interface.

$$x = \left(l^2 - \delta l\right) \Big/ (l - 2\delta_0) \tag{18}$$

$$P = \pi d_f \tau_{fd}(\delta) x \tag{19}$$

$$\tau_{fd}(\delta) = \tau_{f(\mathrm{app})}(\theta)\exp\left[-\eta(\delta - 2\delta_0)^{\alpha}\right] \frac{\left(1 - \exp\left\{\dfrac{-2\nu_f \mu x}{E_f r_f \left[\frac{(1+\nu_m)}{E_m} + \frac{(1-\nu_f)}{E_f}\right]}\right\}\right)}{\left(1 - \exp\left\{\dfrac{-2\nu_f \mu l}{E_f r_f \left[\frac{(1+\nu_m)}{E_m} + \frac{(1-\nu_f)}{E_f}\right]}\right\}\right)} \tag{20}$$

where δ_0 is the end slip of fiber at the onset of full debonding, τ_{fd} is the decaying frictional bond stress, η is the factor reflecting the steepness of the descending branch in fiber pullout curve ($\eta = 0.05$), α is the coefficient determining the initial slope of the frictional slip behavior ($\alpha = 1$), ν_f is the Poisson's ratio of the fiber, and μ is the frictional coefficient at the fiber-matrix interface.

Fig. 12 shows the calculated pullout load–slip responses of straight steel fibers with a length of 13 mm embedded in an ultra-high-strength cementitious matrix in terms of the inclination angle. The variation of the maximum pullout load and slip capacity according to the inclination angle were well replicated by applying Eqs. (12)–(20).

3.2.3. Modeling of the fiber-bridging curve by multiple fibers

In two or three dimensions, the number of fibers per unit area is influenced by the fiber orientation and the embedded length. Fig. 13 shows a fiber arbitrarily located at a distance of z from the matrix crack plane to the centroid of fiber with an inclination angle of θ to the tensile load direction. In three dimensions, the PDFs of θ and z ($p(\theta)$ and $p(z)$) will be $\sin\theta$ and $2/l_f$, respectively. If the inclination angle θ ranges from 0 to $\pi/2$, the distance z will be ranged from 0 to $(l_f/2)\cos\theta$, since the embedded length of fiber cannot be less than 0. Therefore, the number of fibers per unit area is given by

$$N_b = N_{1D} \int_0^{\pi/2} \int_0^{l_f/2} p(l)p(\theta)\cos\theta \, dl \, d\theta \tag{21}$$

where N_{1D} is the number of fibers per unit area in one dimension ($N_{1D} = V_f/A_f$) and $p(l)$ is the PDF for embedment length.

The resistance force of a single fiber at the crack plane is given as a function of the inclination angle θ, the embedded length l, and the amount of slip δ. Thus, the bridging stress of the composites σ_b can be expressed as

$$\sigma_b(\delta) = \frac{4V_f}{\pi d_f^2} \int_0^{\pi/2} \int_0^{l_f/2} P(\theta, l, \delta)p(l)p(\theta)\cos\theta \, dl \, d\theta \tag{22}$$

Since the fiber bridging stress is strongly influenced by the number of fibers, the actual number of fibers obtained from the image analysis needs to be used in order to simulate more accurately the fiber bridging behavior. Therefore, in this study, the fiber number coefficient α_{nf} was introduced, using Eq. (23) [40].

$$\alpha_{nf} = \frac{\pi d_f^2 N_m}{4V_f A_{im} \int_0^{\pi/2} \int_0^{l_f/2} p(l)p(\theta)\cos\theta \, dl \, d\theta} \tag{23}$$

where N_m is the number of fibers measured by using image analysis and A_{im} is the total image area.

Therefore, the actual fiber bridging curve is expressed by

$$\sigma_b(\delta) = \alpha_{nf} \frac{4V_f}{\pi d_f^2} \int_0^{\pi/2} \int_0^{l_f/2} P(\theta, l, \delta)p(l)p(\theta)\cos\theta \, dl \, d\theta \tag{24}$$

The pullout load of the fiber embedded in a plain matrix is different to that of the fiber embedded in the composites (matrix with fibers). According to test results of Markovic [41], the inclusion of fibers in the plain matrix increased the maximum pullout force. In his study, the mix proportion (W/B of 0.2) and type of straight steel fiber (l_f/d_f = 13/0.2 mm/mm) were similar to those used in this study. Thus, the pullout force of the composites $P(\theta, l, \delta)$ is recalculated by adopting coefficient α_f, as follows:

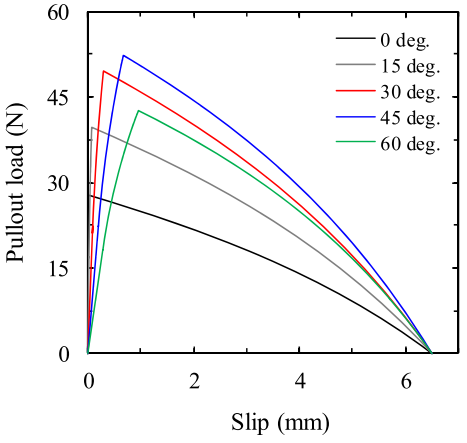

Fig. 12. Analytical pullout responses of straight steel fibers (S13) in ultra-high-strength cementitious matrix with various inclination angles.

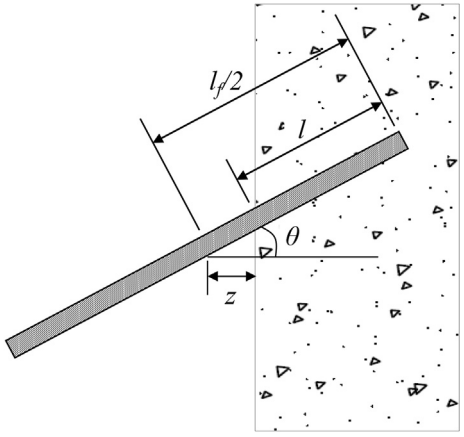

Fig. 13. Embedment length with an inclination angle.

$$P(\theta, l, \delta) = \alpha_f P_{pullout}(\theta, l, \delta) \quad (25)$$

where α_f is the coefficient representing the relationship between the fiber pullout behaviors in the actual composites and in the plain matrix. $\alpha_f = 1.25$ was applied to UHPFRC in accordance with Kang and Kim [16].

The fiber bridging curves obtained by using Eqs. (22)–(25) are shown in Fig. 14. Fiber bridging curves obtained from the assumptions of 2-D and 3-D random fiber orientations were also investigated for comparisons. The measured PDF was adopted for the case of the actual fiber orientation, obtained from the image analysis, while the PDFs of $2/\pi$ and $\sin\theta$ were used for 2-D and 3-D random fiber orientations, respectively.

Regardless of the fiber length, the PDFs assuming 3-D random fiber orientation showed the lowest fiber bridging stress. This indicates that the fibers in UHPFRC were more aligned (better fiber orientation) with the flow direction than the assumption of 3-D random fiber orientation, due to the drag force of the matrix by the flow-velocity gradient. On the other hand, the highest fiber bridging stress was obtained when the measured PDF did not consider α_{nf}. The bridging stresses obtained by using the measured PDFs without consideration for α_{nf} were approximately 30–45% higher than those obtained using the measured PDFs with consideration for α_{nf}. In addition, the bridging strengths calculated based on the measured PDFs considering α_{nf} were quite similar to those predicted by using the PDFs assuming 2-D random fiber orientation. This is in accordance with the findings of Lee et al. [40]. However, smaller crack width at the peak bridging strength was obtained for PDFs assuming random 2-D fiber orientation than those using the measured PDFs. This is because of the different shapes of the PDF curves.

3.2.4. Modeling of the tension-softening curve

Several softening models (i.e., linear, bilinear, and exponential curves) are available for conventional concrete. However, the matrix including steel fibers exhibits different softening behavior to that of the plain concrete. In accordance with a previous study [16], the softening curve of the matrix including steel fibers cannot be predicted by the softening models for the plain concrete proposed by the CEB-FIP code [42]. In general, the fiber bridging stress is activated with an increase in the crack width. This means that the fibers in the fracture process zone (FPZ) do not contribute to the fiber bridging stress. However, they can resist the localization and extension of matrix micro-cracks in FPZ from the shear stress transfer between the fiber and the matrix, as shown in Fig. 15. Thus, the matrix softening curves should be composed of the pure matrix softening and the fiber resistance effect on the localization and extension of the micro-cracks of matrix in the FPZ. Unfortunately, there is no method for quantitatively evaluate the fiber resistance effect in the FPZ. Thus, following a previous study [16], the matrix softening curve was obtained by subtracting the fiber bridging curve calculated on the basis of the measured PDFs considering α_{nf} from the polylinear tension-softening curve obtained from inverse analysis [12].

The matrix softening curves for UHPFRC are shown in Fig. 16. To consider the matrix softening curve using numerical analysis, a

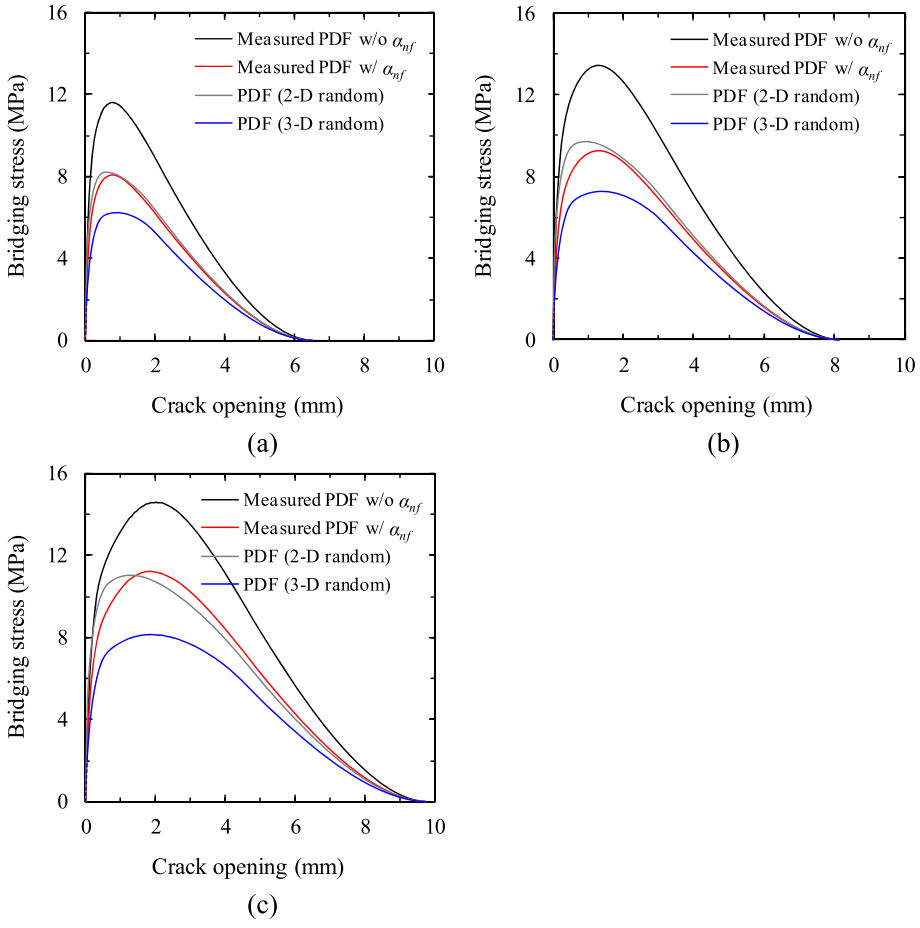

Fig. 14. Fiber bridging curves with various PDFs for fiber orientation; (a) S13, (b) S16.3, (c) S19.5.

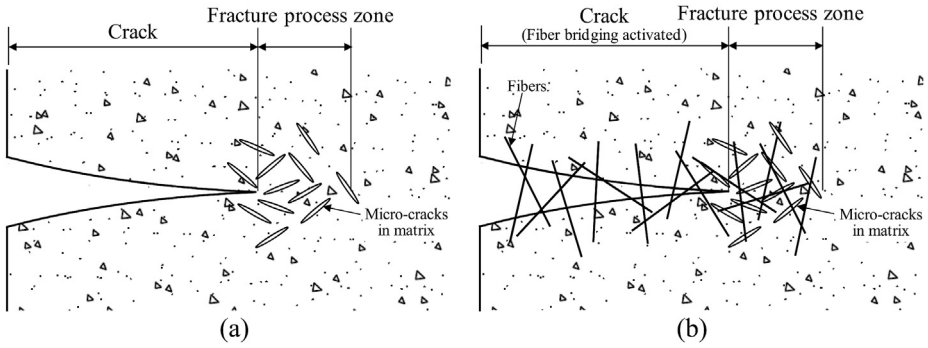

Fig. 15. Schematic description of fracture process in matrix with and without fibers; (a) matrix without fiber, (b) matrix with fibers.

bilinear softening model was adopted, as follows:

$$\sigma_{mt} = f_t\left[1-(1-a)\frac{w}{w_1}\right] \quad \text{for } af_t \le \sigma_{mt} \le f_t \tag{26}$$

$$\sigma_{mt} = \frac{af_t}{w_c - w_1}(w_c - w) \quad \text{for } 0 \le \sigma_{mt} \le af_t \tag{27}$$

where the parameters in the bilinear matrix softening curves (a, w_1, and w_c) are summarize in Table 6.

The micromechanics-based tension-softening curves for UHPFRC are shown in Fig. 17. The order of tensile strength is as follows; 2-D random fiber orientation > actual fiber orientation from image analysis > 3-D random fiber orientation, regardless of the fiber length. For example, the tensile strength of S19.5 calculated on the basis of the PDF assuming 2-D random fiber orientation was found to be 13.7 MPa, approximately 12–25% higher than those calculated on the basis of the PDFs using image analysis and assuming 3-D random fiber orientation. In addition, higher tensile strength and larger crack widths at both the peak strength and the ultimate (tensile stress equals to zero) were obtained with an increase in the fiber length. Thus, it can be concluded that the use of longer steel fibers leads to better flexural performance than that of shorter steel fibers [25], because of the improved fiber-bridging capacity at the crack surfaces.

In order to compare the tensile-softening curves obtained from the micromechanics-based analyses with those obtained from previous models, various tension-softening models suggested by several researchers [12,19–22] were considered. JSCE [19], Habel and Gauvreau [20], and Yoo et al. [21] proposed bilinear tensile stress-COD (σ-w) models with different parameters for UHPFRC containing 2 vol% of short straight steel fibers (l_f ranging from 13 mm to 15 mm), while Kang et al. [22] and Yoo et al. [12] suggested trilinear tensile σ-w models for UHPFRC with various volume fractions and lengths of straight steel fibers, respectively. The detailed equations for all suggested softening models can be found in the Appendix. The parameters suggested by the researchers are also summarized in Table A1, and the calculated tensile σ-w models are shown in Fig. 18.

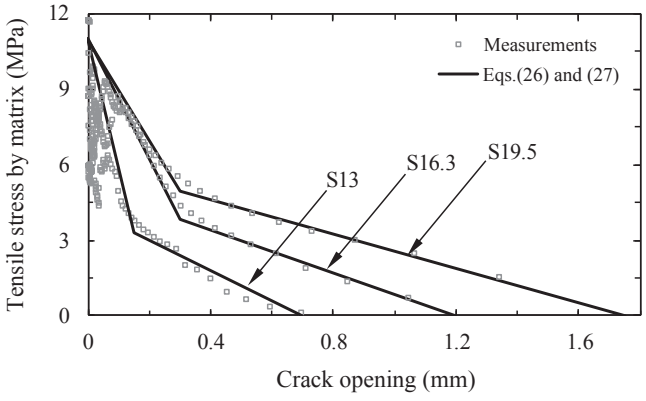

Fig. 16. Matrix softening curves for UHPFRC according to fiber length.

Table 6
Parameters of matrix softening curve.

Name	a	w_1	w_c
S13	0.30	0.15	0.70
S16.3	0.35	0.30	1.20
S19.5	0.45	0.30	1.75

It is obvious that according to the researchers, the suggested tension-softening models were completely different. Since JSCE [19], Habel and Gauvreau [20], and Yoo et al. [21] suggested the bilinear models only for UHPFRC containing short straight steel fibers at the V_f of 2%, one type of bilinear model was adopted regardless of fiber length. Although Kang et al. [22] proposed the trilinear softening model for UHPFRC including short straight steel fibers with various fiber volume fractions, the effect of fiber length on the tension-softening model was able to be considered due to the parameter of ultimate COD (w_c). Thus, only the ultimate COD value was changed according to the fiber length. On the other hand, Yoo et al. [12] proposed a generalized trilinear softening model, applicable for all types of UHPFRC with various lengths and orientations of straight steel fibers, so it was able to consider the implication of fiber length on the softening behavior. Based on their model, the tensile strength and ultimate COD were obviously influenced by the fiber length: a higher tensile strength and COD were obtained with increasing the fiber length.

3.3. Sectional analysis

In order to verify the suggested micromechanics-based tension-softening curves and previous models, sectional analysis was performed. Sectional analysis is a very useful and powerful method for modeling the flexural behavior of concrete beams presenting a single dominant crack [43]. Since sectional analysis can take into account the realistic stress-strain (or stress-COD) relationship under compression and tension, several researchers have adopted this analysis to predict the flexural behavior of FRC beams [43–45]. Since the UHPFRC beams used in this study are subjected to a center point loading and include 30-mm notch at mid-length, a single dominant flexural crack was formed for all test series, as shown in Fig. 4. For this reason, the failure configuration of the UHPFRC beam with a center point load is simplified as shown in Fig. 19. The

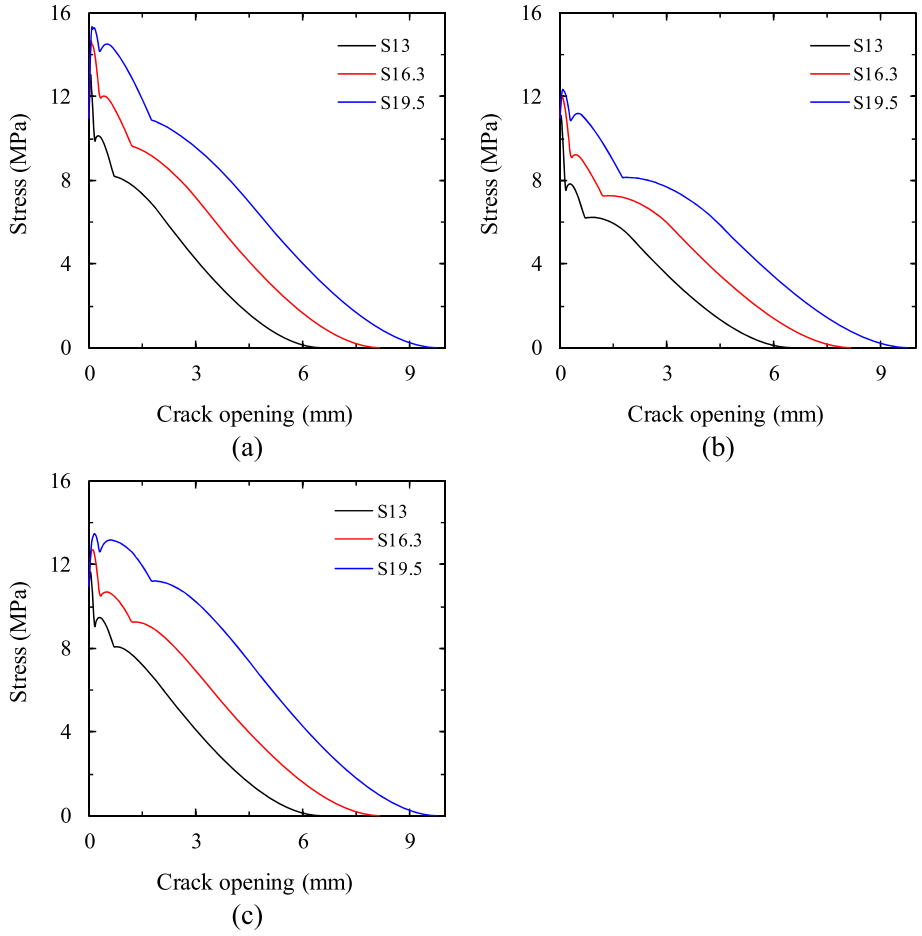

Fig. 17. Tension-softening curves for UHPFRC; (a) 2-D random fiber orientation, (b) 3-D random fiber orientation, (c) actual fiber orientation from image analysis.

cracked section at mid-length is assumed to be acting as a plastic hinge, and the total axial shortening of the top fiber in the beam is given by

$$\Delta_0 = \int_0^L \varepsilon_x dx = \frac{1}{2}\varepsilon_{cf} L \tag{28}$$

where Δ_0 is the total axial shortening of the beam at the topmost fiber, L is the span length, ε_x is the axial strain of the beam at the topmost fiber, and ε_{cf} is the axial strain at mid-length of the beam at the topmost fiber.

Based on the geometrical conditions, the incremental rotation angle $d\theta$, mid-span deflection $d\delta$, and CMOD $dCMOD$ are expressed, as follows

$$d\theta \approx \frac{\Delta_0}{2c} \tag{29}$$

$$d\delta = d\theta \frac{L}{2} \tag{30}$$

$$dCMOD = 2[d\theta(h - c)] \tag{31}$$

where c is the neutral axis depth and h is the height of the beam.

The stress distribution along the uncracked depth is given as a function of the strain distribution. The strain distribution was assumed to be linear based on the assumption that the plane section remains plane. In general, UHPFRC shows a very linear relationship for both compressive stress-strain before failure and tensile stress-strain before cracking [8]. Thus, the linear compressive and tensile stress-strain models for UHPFRC at uncracked section were used in this study, as follows

$$f_c = E_c \varepsilon_c \tag{32}$$

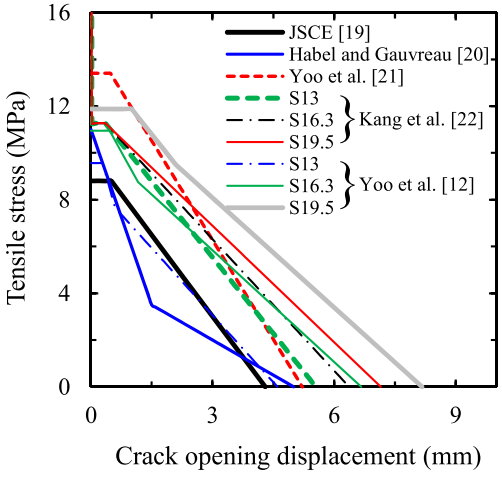

Fig. 18. Summary of bi or trilinear tension-softening models.

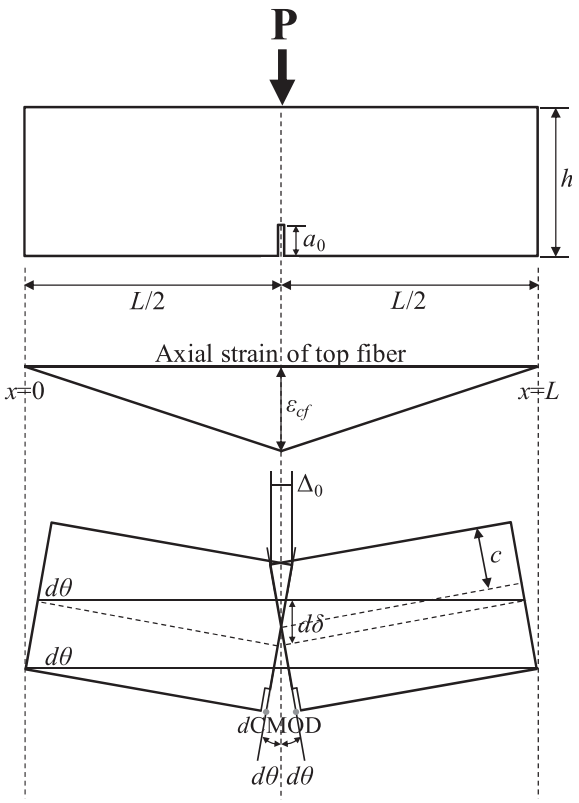

Fig. 19. Idealized failure mode of FRC beam under center point load.

where f_c is the stress of concrete, E_c is the elastic modulus of concrete, and ε_c is the strain of concrete.

The tension-softening curve is composed of matrix softening and fiber bridging curves. The stress distribution by matrix softening is easily considered along the crack depth because it is expressed by simple equations (Eqs. (26) and (27)). However, the fiber bridging curve along the crack depth is difficult to be considered by sectional analysis on account of its complicated shape. Thus, although it is the best way to consider the actual fiber bridging curve obtained from the micromechanical approach in the sectional analysis, simple equations for simulating ascending and descending branches of fiber bridging curve were alternatively adopted.

For the ascending branch, Eq. (33) was adopted based on Gopalaratnam and Shah's model [46], which was suggested for the stress-COD relationship of the softening curve in concrete.

$$\sigma_b = \sigma_{ub}\left(1 - e^{-aw^b}\right) \tag{33}$$

where σ_b is the fiber bridging stress, σ_{ub} is the maximum fiber bridging strength, a and b are empirical coefficients, and w is the crack width.

Fig. 20(a) shows the prediction of the ascending branch of fiber bridging curve from Eq. (33). For all test series, the coefficient of determination (R^2) was found to be higher than 0.99. Thus, Eq. (33) was proper for modeling the ascending branch of the UHPFRC fiber bridging curves. The empirical coefficients a and b, obtained by the least-square method, for all test series are listed in Table 7.

For the descending branch, the simple linear softening curve suggested by Kang and Kim [47] was applied, as follows

$$\sigma_b = \frac{4\left(l_f/2\right)V_f\tau_f}{\pi d_f}\left(1 - \frac{w - w_s}{0.85\left(l_f/2\right) - w_s}\right) \text{ for } w \le 0.85\left(l_f/2\right) \tag{34}$$

$$\sigma_b = 0 \text{ for } w > 0.85\left(l_f/2\right) \tag{35}$$

where w_s is the crack width when the fiber starts to slide at the interface.

The comparison between the micromechanics-based fiber bridging curve and the modeled curve is shown in Fig. 20(b). The solid line indicates the micromechanics-based fiber bridging curve, while the dotted line indicates the modeled curve. The overall fiber bridging curves calculated using Eqs. (33)–(35) showed quite good agreement with the curve obtained from the micromechanics-based approach. Therefore, the modeled fiber bridging curve was incorporated into the sectional analysis algorithm in lieu of that obtained from the micromechanics-based analysis.

The modeled fiber bridging curves are shown in Fig. 21. Regardless of the fiber length, the fiber bridging strength obtained using the PDFs assuming 3-D random fiber orientation was lower than that obtained by the PDFs measured from image analysis. In contrast, the PDFs assuming 2-D random fiber orientation exhibited similar maximum bridging strength with the measured PDFs. Thus, it is concluded that if the PDF for fiber orientation is not obtained

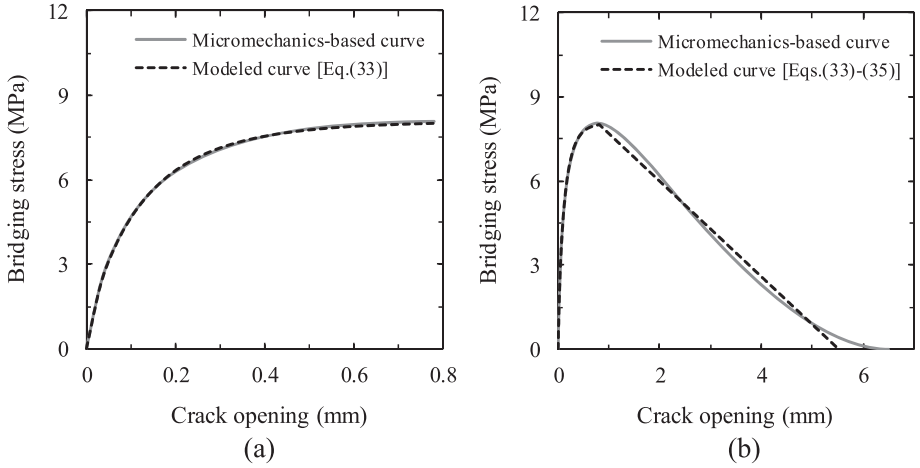

Fig. 20. Comparison of fiber bridging curves calculated by micromechanics-based analysis and Eqs. (33)–(35) (l_f = 13 mm); (a) initial behavior, (b) overall behavior.

Table 7
Summary of empirical coefficients *a* and *b*.

Name		*a*	*b*
S13	Measured PDF	5.87	0.834
	2-D random	6.59	0.727
	3-D random	5.90	0.866
S16.3	Measured PDF	3.75	0.782
	2-D random	5.27	0.726
	3-D random	4.22	0.827
S19.5	Measured PDF	2.75	0.742
	2-D random	4.27	0.707
	3-D random	3.20	0.775

from image analysis, a 2-D random fiber orientation can be used as a substitute for small-sized UHPFRC beams without internal reinforcements.

Synthetically, the material model for UHPFRC in compression and tension is shown in Fig. 22. This model is divided into two categories: (1) the uncracked region and (2) the cracked region. A schematic diagram of the stress, strain, and crack width distributions at the cross-section is shown in Fig. 23. The internal resisting moment M is calculated through an iterative procedure to determine the appropriate neutral axis depth in terms of the force equilibrium condition, as follows

$$\int_0^{c'} f_c dA + \sum_{i=1}^{n} \sigma_{ct,i} = 0 \tag{36}$$

$$M = \int_0^{c'} f_c y dA + \sum_{i=1}^{n} \sigma_{ct,i} y_i \tag{37}$$

where σ_{ct} is the summation of matrix softening and fiber bridging stresses.

The matrix softening and fiber bridging stresses can be obtained from the stress-COD relationship. If the width of the notch (which represents only 1% of the total beam length) is assumed to be negligible, the crack width at the i th layer can be expressed by

$$w_i = \frac{CMOD}{h - c} y_i \tag{38}$$

From the moment M calculated by Eq. (37), the applied load P can be obtained from the following equation.

$$P = \frac{4M}{L} \tag{39}$$

The algorithm of sectional analysis for predicting the flexural response of UHPFRC beams is shown in Fig. 24. Details of the analytical procedures are available elsewhere [8]. Fig. 25 shows the comparison of load-CMOD curves obtained from the experiments and sectional analyses incorporating micromechanics-based tension-softening curves. The analytical predictions using the fiber bridging curve on the basis of the PDFs measured from image analysis agree fairly well with the present test data. In particular, the maximum load and the corresponding CMOD were almost perfectly predicted. However, the prediction exhibited a slightly

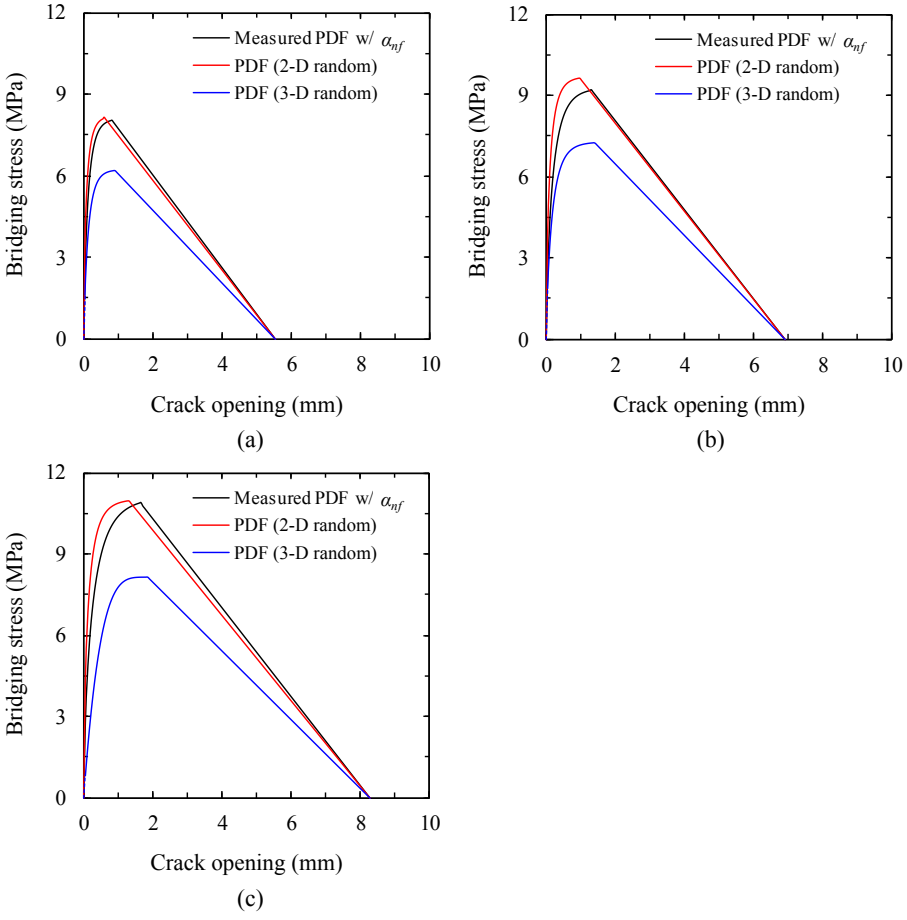

Fig. 21. Modeled fiber bridging curves; (a) S13, (b) S16.3, (c) S19.5.

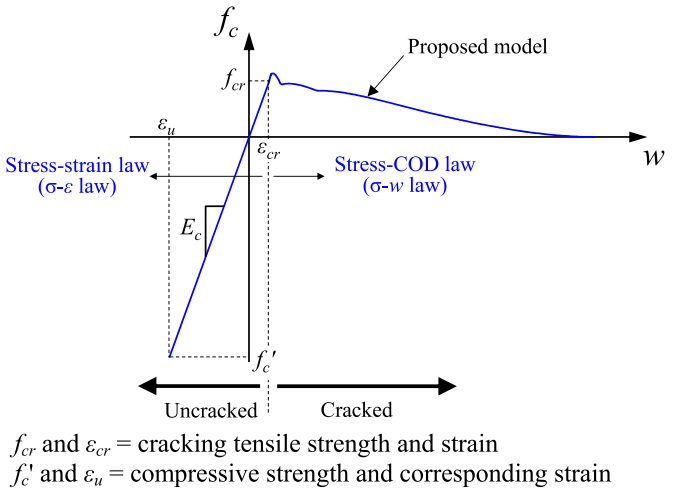

Fig. 22. Material models for UHPFRC under compression and tension.

higher load resistance at certain CMOD values in the post-peak softening region. The analytical predictions with the fiber bridging curve on the basis of the PDFs assuming 2-D random fiber orientation showed slightly higher maximum load and post-peak load resistance than the present test data. In contrast, the predictions based on the PDFs assuming 3-D random fiber orientation exhibited much lower maximum load than the test data, regardless of the fiber length. From the results, it is concluded that the micromechanics-based sectional analyses using the PDFs for fiber orientation obtained from image analysis predict the flexural behavior of UHPFRC beams with various fiber lengths well. In addition, the assumption of 2-D random fiber orientation is more appropriate to predict the flexural behavior of UHPFRC beams than the assumption of 3-D random fiber orientation.

Fig. 26 also exhibits the comparison of experimental results and predicted values obtained from previous tension-softening models [12,19–22]. For the specimen S13, the sectional analyses incorporating tension-softening models suggested by the present study, JSCE [19], and Yoo et al. [12] provided good agreement with the overall flexural behavior obtained from experiments. The analysis including Habel and Gauvreau's model [20] well predicted the pre-peak flexural behavior as well as the flexural strength, but it exhibited steeper decrease in the load carrying capacity after the peak point as compared with the test data. On the other hand, the analytical results incorporating tension-softening models from Kang et al. [22] and Yoo et al. [21] significantly overestimated the

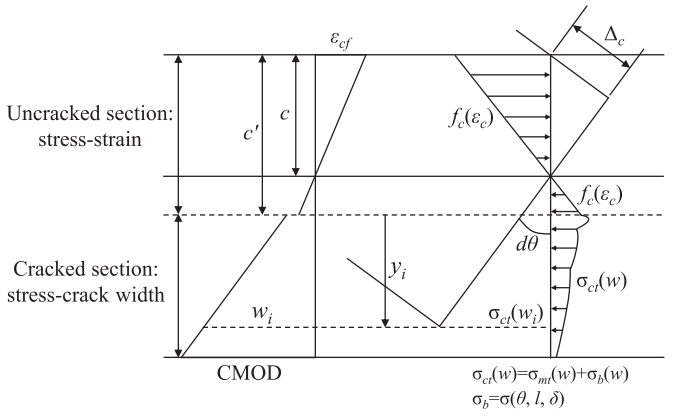

Fig. 23. Schematic description of uncracked and cracked sections.

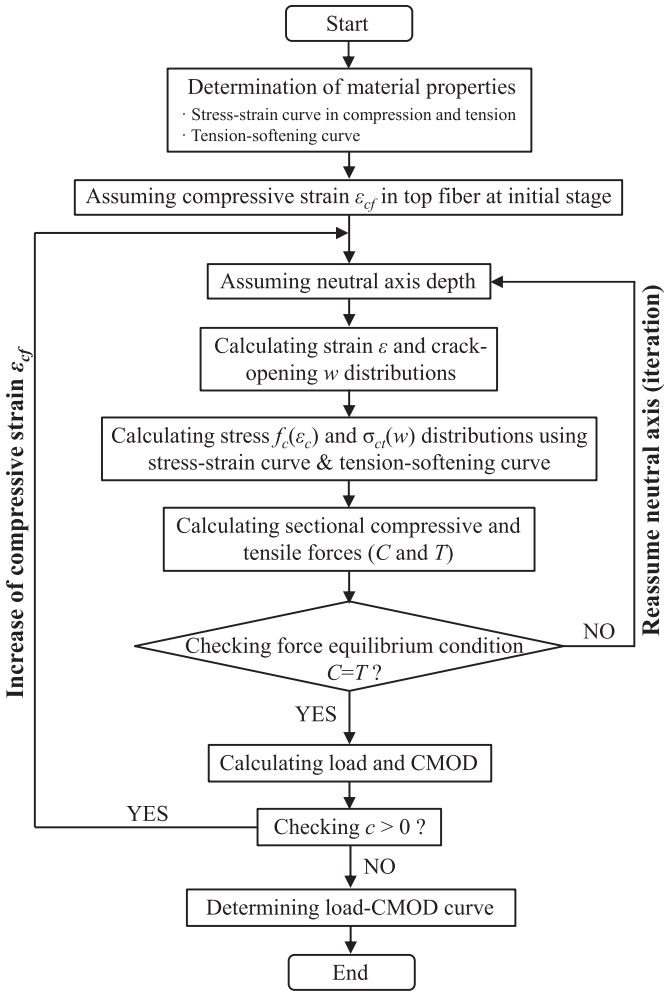

Fig. 24. Algorithm for sectional analysis.

flexural strength as compared to the test data. This is caused by the fact that the tension-softening models suggested by Kang et al. [22] and Yoo et al. [21] were based on the flexural test results of UHPFRC beams, fabricated by a placement method different to that adopted in this study. The different placement method may have caused the discrepancy between the test data and the predictive values, because of the different fiber orientations.

The analytical results considering the tension-softening models suggested by JSCE [19] and Habel and Gauvreau [20] obviously underestimated the flexural strength than the test data for the specimens S16.3 and S19.5. This is because they suggested the models only based on the test data obtained for UHPFRC including short straight steel fibers. The analytical results considering the models proposed by Kang et al. [22] and Yoo et al. [21] exhibited good agreement with the test data of S16.3 and S19.5, respectively. However, it seems to be a coincidence because their models were suggested for UHPFRC incorporating short straight steel fibers with a length of 13 mm.

Yoo's generalized softening model [12] presented quite a good agreement with the test data regardless of the fiber length, because their model was proposed based on the test results of UHPFRCs with various lengths and orientations of straight steel fibers. However, the micromechanical approach incorporating the actual PDF of fiber orientation exhibited the best prediction to the test data regardless of the fiber length. From these observations, it is noted that most of the previous models are only applicable to a specific type of UHPFRC

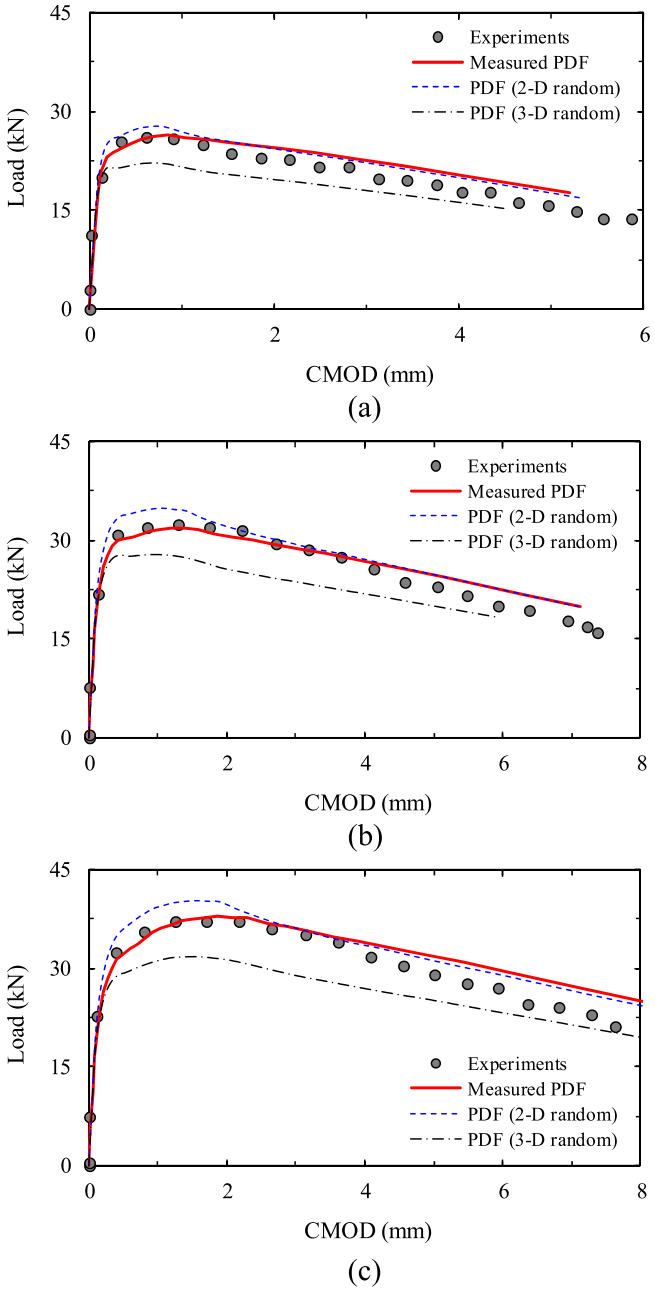

Fig. 25. Comparison of experimental and analytical results; (a) S13, (b) S16.3, (c) S19.5.

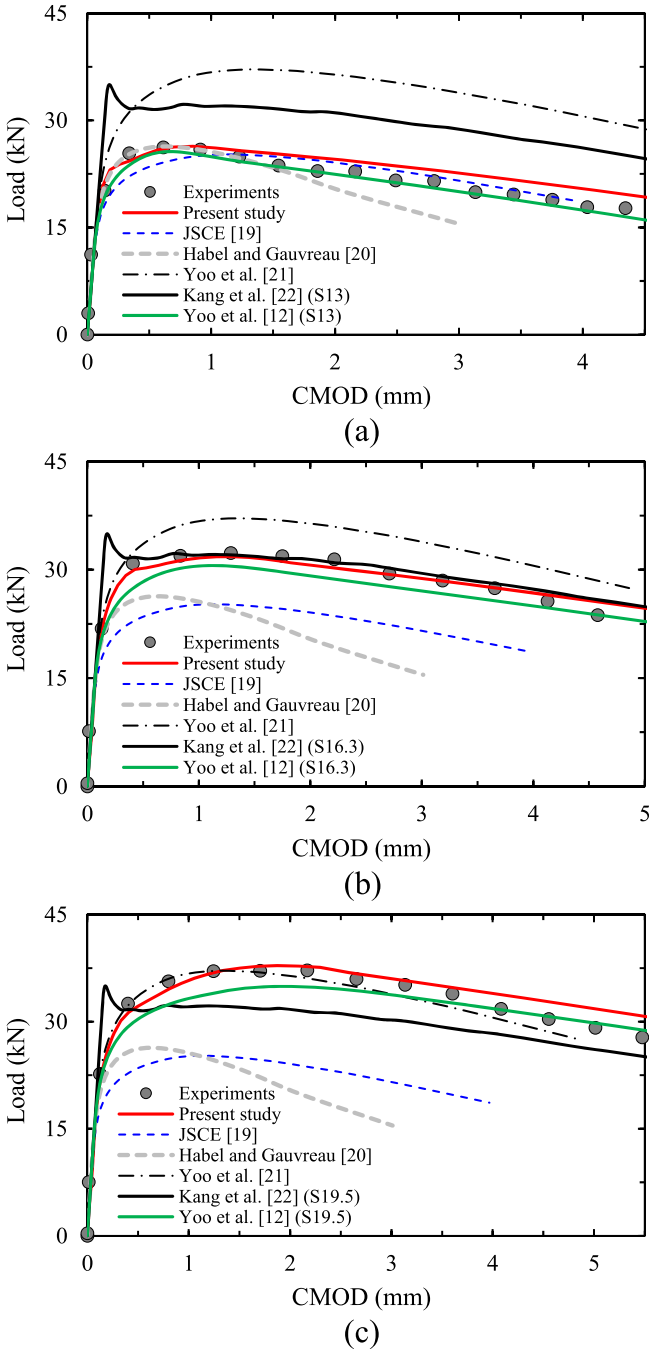

Fig. 26. Comparison of experimental results and predictive values from various tension-softening models; (a) S13, (b) S16.3, (c) S19.5 (Note: Present study indicates the micromechanical analysis incorporating fiber bridging curve from the measured PDF of fiber orientation).

and not generally applied for various types of UHPFRC with different lengths, shapes, and volume fractions of steel fibers. Accordingly, the micromechanical approach introduced in this study can be one of the solutions to overcome the drawbacks of previous models and generally applied for various types of UHPFRC.

4. Conclusions

The flexural behaviors of UHPFRC beams including straight steel fibers with various lengths were numerically investigated. For the numerical analysis, sectional analyses incorporating linear compressive and tensile models before cracking and tension-softening curves obtained from micromechanical approach and previous models were adopted and verified through a comparison with the test data. From the above discussions, the following conclusions are made:

1) The use of longer steel fibers resulted in better flexural performance, but poorer fiber orientation, compared to that with shorter steel fibers. In contrast, the initial and descending slopes of the flexural load-CMOD curve, the fiber dispersion, and number of fibers were not significantly affected by the fiber length.
2) To obtain tension-softening curve, the fiber bridging curve was calculated based on the pullout model of straight steel fibers embedded in an ultra-high-strength cementitious matrix and a bilinear matrix softening curve was adopted. In particular, the fiber bridging strength was influenced by the fiber length and orientation. Higher fiber bridging strength was obtained with a

higher fiber length. The order of fiber bridging strength was also found to be 2-D random fiber orientation > actual fiber orientation by image analysis > 3-D random fiber orientation.

3) The sectional analyses incorporating the fiber bridging curve based on the PDFs using fiber orientation from image analysis exhibited fairly good agreement with the test data. The use of PDFs assuming 2-D random fiber orientation showed slightly higher load carrying capacity, whereas the use of PDFs assuming 3-D random fiber orientation exhibited much lower load carrying capacity than the experimental results. From these results, it was concluded that the micromechanics-based sectional analysis using the PDFs obtained from image analysis is most suitable for predicting the flexural response of UHPFRC beams. However, if the actual PDF is not obtained from the image analysis, the assumption of 2-D random fiber orientation can be adopted as a substitute to predict the flexural behavior. This is more accurate than the assumption of 3-D random fiber orientation.
4) Most of the previously suggested tension-softening models were only appropriate to a specific type of UHPFRC, and they were not generally applied for UHPFRCs with various lengths, shapes, and volume contents of fibers. This limitation was able to be overcome by using the micromechanical approach although it required quite complicated equations for modeling fiber bridging curve.

Acknowledgements

This work was supported by the National Research Foundation of Korea (NRF) grant funded by the Korea government (MEST) (NRF-2016R1A2B3011392).

Appendix

Previous tensile stress-COD models for UHPFRC

- Bilinear models

JSCE [19], Habel and Gauvreau [20], and Yoo et al. [21] proposed a bilinear stress-COD model (Eqs. (A1) and (A2)), and the parameters suggested are all summarized in Table A1.

$$\sigma = f_t - (f_t - f_1)\frac{w}{w_1} \quad \text{for} \quad w < w_1 \tag{A1}$$

$$\sigma = f_1\left(1 - \frac{w - w_1}{w_c - w_1}\right) \quad \text{for} \quad w_1 \le w < w_c \tag{A2}$$

where σ is the tensile stress, f_t is the tensile strength, f_1 is the tensile stress at a kink point, w is the COD, w_1 is the COD at f_1, and w_c is the ultimate COD at $\sigma = 0$.

- Trilinear models

Kang et al. [22] proposed a trilinear stress-COD model having an initial softening branch due to matrix cracking, a fiber bridging plateau, and a final softening branch, as follows

$$\sigma = -\frac{f_t - f_1}{w_1}w + f_t \quad \text{for} \quad w < w_1 \tag{A3}$$

$$\sigma = f_1 \quad \text{for} \quad w_1 < w < w_2 \tag{A4}$$

$$\sigma = -\frac{f_1}{w_c\text{-}w_2}(w - w_c) \quad \text{for} \quad w_2 < w < w_c \tag{A5}$$

$$\sigma = 0 \quad \text{for} \quad w_c < w \tag{A6}$$

where σ is the tensile stress, f_t is the tensile strength, f_1 is the tensile stress at the region of fiber bridging plateau, w is the COD, w_1 is the COD at the beginning of f_1, w_2 is the COD at the end of f_1, and w_c is the ultimate COD at $\sigma = 0$.

Based on the numbers of flexural tests and inverse analyses, they suggested the following equations for predicting the parameters in Eqs. (A3)–(A6), considering the volume fraction of short straight steel fibers.

$$f_t = a_{f_t}V_f + b_{f_t} \tag{A7}$$

$$f_1 = a_{f_1}V_f + b_{f_1} \tag{A8}$$

$$w_1 = b_{w_1} \tag{A9}$$

$$w_2 - w_1 = a_{w_2}\left(1 - e^{-b_{w_2}V_f}\right) \tag{A10}$$

$$\begin{cases} w_c = \dfrac{l_f}{2} & \text{for} \quad V_f < b_{w_c} \\ w_c = \dfrac{l_f}{2}e^{-(V_f - b_{w_c})} + a_{w_c}\left(1 - e^{-(V_f - b_{w_c})}\right) & \text{for} \quad V_f \ge b_{w_c} \end{cases} \tag{A11}$$

where V_f is the fiber volume fraction by percent and l_f is the fiber length. Experimental coefficients $a_{ft} = 7.09$, $b_{ft} = 16.2$, $a_{f1} = 3.79$, $b_{f1} = 3.69$, $b_{w1} = 0.0242$, $a_{w2} = 0.5$, $b_{w2} = 0.54$, $a_{wc} = 4.64$, and $b_{wc} = 1.29$ were proposed.

According to Eqs. (A7)–(A11), the parameters in Eqs. (A3)–(A6) were calculated and summarized in Table A1.

Yoo et al. [12] suggested a generalized trilinear softening model, which is applicable for UHPFRC with various lengths and orientations of straight steel fibers. To obtain the generalized model, they [12] used dimensionless parameters, i.e., σ/f_t and w/w_{ch}, where w_{ch} is the ratio between fracture energy and tensile strength ($= G_F/f_t$), similar to that adopted by Bažant and Zi [48]. The generalized trilinear tension softening model proposed by Yoo et al. [12] is as follows

$$\sigma = f_t \quad \text{for} \quad w < w_1 \tag{A12}$$

$$\sigma = f_t\left(1 - 0.2\frac{w - w_1}{w_2 - w_1}\right) \quad \text{for} \quad w_1 < w \le w_2 \tag{A13}$$

$$\sigma = 0.8f_t\left(\frac{w_c - w}{w_c - w_2}\right) \quad \text{for} \quad w_2 < w \le w_c \tag{A14}$$

$$w_1 = 0.15\frac{G_F}{f_t} \tag{A15}$$

$$w_2 = 2\frac{G_F}{f_t} - 0.8w_c \tag{A16}$$

$$w_c = 2\frac{G_F}{f_t} \tag{A17}$$

where σ is the tensile stress, f_t is the tensile strength, w is the COD, w_1 is the COD at the end of initial plateau with f_t, w_2 is the COD at the kink point, G_F is the fracture energy, and w_c is the ultimate COD at $\sigma = 0$.

The parameters used in Eqs. (A12)–(A17) are also given in Table A1.

Table A1
Summary of previous tensile stress-COD models for UHPFRC

	Model type	Parameters
JSCE [19]	Bilinear	$f_t = f_1 = 8.8$ MPa, $w_1 = 0.5$ mm, and $w_c = 4.3$ mm
Habel and Gauvreau [20]	Bilinear	$f_t = 11$ MPa, $f_1 = 3.5$ MPa, $w_1 = 1.5$ mm, and $w_c = 5.0$ mm
Yoo et al. [21]	Bilinear	$f_t = f_1 = 13.4$ MPa, $w_1 = 0.48$ mm, and $w_c = 5.22$ mm
Yoo et al. [12]	Trilinear	S13: $f_t = 9.56$ MPa, $w_1 = 0.29$ mm, $w_2 = 0.60$ mm, $w_c = 4.60$ mm, and $G_F = 21.80$ N/mm
		S16.3: $f_t = 10.95$ MPa, $w_1 = 0.46$ mm, $w_2 = 1.16$ mm, $w_c = 6.67$ mm, and $G_F = 37.09$ N/mm
		S19.5: $f_t = 11.88$ MPa, $w_1 = 1.00$ mm, $w_2 = 2.09$ mm, $w_c = 8.17$ mm, and $G_F = 53.55$ N/mm
Kang et al. [22]	Trilinear	S13: $f_t = 30.38$ MPa, $f_1 = 11.27$ MPa, $w_1 = 0.0242$ mm, $w_2 = 0.354$ mm, and $w_c = 5.55$ mm
		S16.3: $f_t = 30.38$ MPa, $f_1 = 11.27$ MPa, $w_1 = 0.0242$ mm, $w_2 = 0.354$ mm, and $w_c = 6.37$ mm
		S19.5: $f_t = 30.38$ MPa, $f_1 = 11.27$ MPa, $w_1 = 0.0242$ mm, $w_2 = 0.354$ mm, and $w_c = 7.15$ mm

References

[1] A. Bentur, S. Mindess, Fibre Reinforced Cementitious Composites, E&FN Spon, 2007.
[2] N. Banthia, N. Nandakumar, Crack growth resistance hybrid fiber reinforced cement composites, Cem. Concr. Compos 25 (1) (2003) 3–9.
[3] D.Y. Yoo, H.O. Shin, J.Y. Lee, Y.S. Yoon, Enhancing cracking resistance of ultra-high-performance concrete slabs using steel fibres, Mag. Concr. Res. 67 (10) (2015) 487–495.
[4] D.Y. Yoo, Y.S. Yoon, N. Banthia, Flexural response of steel-fiber-reinforced concrete beams: effects of strength, fiber content, and strain-rate, Cem. Concr. Compos 64 (2015) 84–92.
[5] V.C. Li, H. Stang, H. Krenchel, Micromechanics of crack bridging in fibre-reinforced concrete, Mater Struct. 26 (8) (1993) 486–494.
[6] D.Y. Yoo, S.T. Kang, J.H. Lee, Y.S. Yoon, Effect of shrinkage reducing admixture on tensile and flexural behaviors of UHPFRC considering fiber distribution characteristics, Cem. Concr. Res. 54 (2013) 180–190.
[7] T. Makita, E. Brühwiler, Tensile fatigue behaviour of ultra-high performance fibre reinforced concrete (UHPFRC), Mater Struct. 47 (3) (2014) 475–491.
[8] D.Y. Yoo, Performance Enhancement of Ultra-high-performance Fiber-reinforced Concrete and Model Development for Practical Utilization, Korea University, Seoul, Korea, 2014, p. 586. Ph.D. thesis.
[9] K. Wille, D.J. Kim, A.E. Naaman, Strain-hardening UHP-FRC with low fiber contents, Mater Struct. 44 (3) (2011) 583–598.
[10] S. Aydın, B. Baradan, The effect of fiber properties on high performance alkali-activated slag/silica fume mortars, Compos Part B Eng. 45 (1) (2013) 63–69.
[11] D.Y. Yoo, Y.S. Yoon, Structural performance of ultra-high-performance concrete beams with different steel fibers, Eng. Struct. 102 (2015) 409–423.
[12] D.Y. Yoo, S.T. Kang, Y.S. Yoon, Effect of fiber length and placement method on flexural behavior, tension-softening curve, and fiber distribution characteristics of UHPFRC, Constr. Build. Mater 64 (2014) 67–81.
[13] B.A. Graybeal, Flexural behavior of an ultrahigh-performance concrete I-girder, J. Bridge Eng. 13 (6) (2008) 602–610.
[14] N.T. Tran, T.K. Tran, D.J. Kim, High rate response of ultra-high-performance fiber-reinforced concretes under direct tension, Cem. Concr. Res. 69 (2015) 72–87.
[15] Z.P. Bažant, J. Planas, Fracture and Size Effect in Concrete and Other Quasi-brittle Materials, CRC Press, New York, 1997, p. 616.
[16] S.T. Kang, J.K. Kim, The relation between fiber orientation and tensile behavior in an ultra high performance fiber reinforced cementitious composites (UHPFRCC), Cem. Concr. Res. 41 (10) (2011) 1001–1014.
[17] K. Habel, E. Denarié, E. Brühwiler, Structural response of elements combining ultrahigh-performance fiber-reinforced concretes and reinforced concrete, J. Struct. Eng. 132 (11) (2006) 1793–1800.
[18] K. Wille, N.V. Tue, G.J. Parra-Montesinos, Fiber distribution and orientation in UHP-FRC beams and their effect on backward analysis, Mater Struct. 47 (11) (2014) 1825–1838.
[19] JSCE, Recommendations for Design and Construction of Ultra-high Strength Fiber Reinforced Concrete Structures (Draft), Japan Society of Civil Engineers, Tokyo, Japan, 2004.
[20] K. Habel, P. Gauvreau, Response of ultra-high performance fiber reinforced concrete (UHPFRC) to impact and static loading, Cem. Concr. Compos 30 (10) (2008) 938–946.
[21] D.Y. Yoo, J.H. Lee, Y.S. Yoon, Effect of fiber content on mechanical and fracture properties of ultra high performance fiber reinforced cementitious composites, Compos Struct. 106 (2013) 742–753.
[22] S.T. Kang, Y. Lee, Y.D. Park, J.K. Kim, Tensile fracture properties of an ultra high performance fiber reinforced concrete (UHPFRC) with steel fiber, Compos Struct. 92 (1) (2010) 61–71.
[23] ASTM C 39/39M, Standard Test Method for Compressive Strength of Cylindrical Concrete Specimens, ASTM International, West Conshohocken, PA, 2014, pp. 1–7.
[24] JCI-S-002-2003, Method of Test for Load-displacement Curve of Fiber Reinforced Concrete by Use of Notched Beam, Japan Concrete Institute Standard, 2003.
[25] D.Y. Yoo, G. Zi, S.T. Kang, Y.S. Yoon, Biaxial flexural behavior of ultra-high-performance fiber-reinforced concrete with different fiber lengths and placement methods, Cem. Concr. Compos 63 (2015) 51–66.
[26] D.Y. Yoo, N. Banthia, G. Zi, Y.S. Yoon, Comparative biaxial flexural behavior of ultra-high-performance fiber-reinforced concrete panels using two different test and placement methods, J. Test. Eval. (2017), http://dx.doi.org/10.1520/JTE20150275. In-press.
[27] A.E. Naaman, H.W. Reinhardt, Proposed classification of HPFRC composites based on their tensile response, Mater Struct. 39 (5) (2006) 547–555.
[28] KCI, Design Recommendations for Ultra-high Performance Concrete K-UHPC. KCI-M-12–003, Korea Concrete Institute, Seoul, Korea, 2012.
[29] L.X. Zang, J.Z. Lin, T.L. Chan, On the Modelling of Motion of Non-spherical Particles in Two-phase Flow. 6th International Conference on Multiphase Flow, ICMF 2007, Leipzig, Germany, 2007.
[30] L. Ferrara, High performance fiber reinforced self-compacting concrete (HPFR-SCC): a “smart material” for high end engineering applications, in: 3rd International Workshop on Heterogeneous Architectures and Computing, Madrid, 2012, pp. 325–334.
[31] V.C. Li, Y. Wang, S. Backer, A micromechanical model of tension-softening and bridging toughness of short random fiber reinforced brittle matrix composites, J. Mech. Phys. Solids 39 (5) (1991) 607–625.
[32] H.X. Cox, The elasticity and strength of paper and other fibrous materials, Br. J. Appl. Phys. 3 (3) (1952) 72–79.
[33] M.R. Piggott, Load Bearing Fibre Composites, Pergamon Press, Oxford, 1980, p. 277.
[34] V.C. Li, Y. Wang, S. Backer, Effect of inclining angle, bundling and surface treatment on synthetic fiber pull-out from a cement matrix, Compos 21 (2) (1990) 132–140.
[35] Y. Lee, S.T. Kang, J.K. Kim, Pullout behavior of inclined steel fiber in an ultra-high strength cementitious matrix, Const. Build. Mater 24 (10) (2010) 2030–2041.
[36] N. Banthia, J.F. Trottier, Concrete reinforced with deformed steel fibers, Part I: bond-slip mechanisms, ACI Mater J. 91 (5) (1994) 435–446.
[37] E.A. Schauffert, G. Cusatis, D. Pelessone, J.L. O'Daniel, J.T. Baylot, Lattice discrete particle model for fiber-reinforced concrete. II: tensile fracture and multiaxial loading behavior, J. Eng. Mech. 138 (7) (2011) 834–841.
[38] T. Kanda, V.C. Li, Interface property and apparent strength of high-strength hydrophilic fiber in cement matrix, J. Mater Civ. Eng. 10 (1) (1998) 5–13.
[39] A.E. Naaman, G.G. Namur, J.M. Alwan, H.S. Najm, Fiber pullout and bond slip. 1: analytical study, J. Struct. Eng. ASCE 117 (9) (1991) 2769–2790.
[40] B.Y. Lee, Y. Lee, J.K. Kim, Y.Y. Kim, Micromechanics-based fiber bridging analysis of strain-hardening cementitious composite accounting for fiber distribution, Comp. Model. Eng. Sci. 61 (2) (2010) 111–132.
[41] I. Markovic, High-performance Hybrid-fibre Concrete – Development and Utilization, Delft University of Technology, Delft, The Netherlands, 2006, p. 211. Ph.D. thesis.
[42] CEB-FIP, CEB-FIP, Model Code 1990, Thomas Telford, London, 1993.
[43] H.S. Armelin, N. Banthia, Predicting the flexural postcracking performance of steel fiber reinforced concrete from the pullout of single fibers, ACI Mater J. 94 (1) (1997) 18–31.
[44] B.H. Oh, D.G. Park, J.C. Kim, Y.C. Choi, Experimental and theoretical investigation on the postcracking inelastic behavior of synthetic fiber reinforced concrete beams, Cem. Concr. Res. 35 (2) (2005) 384–392.
[45] D.Y. Yoo, Y.S. Yoon, N. Banthia, Predicting the post-cracking behavior of normal- and high-strength steel-fiber-reinforced concrete beams, Constr. Build. Mater 93 (2015) 477–485.
[46] V.S. Gopalaratnam, S.P. Shah, Softening response of plain concrete in direct tension, ACI J. 82 (3) (1985) 310–323.
[47] S.T. Kang, J.K. Kim, Investigation on the flexural behavior of UHPCC considering the effect of fiber orientation distribution, Const. Build. Mater 28 (1) (2012) 57–65.
[48] Z.P. Bažant, G. Zi, Asymptotic stress intensity factor density profile for smeared-tip method for cohesive fracture, Int. J. Fract. 119 (2) (2003) 145–159.